Geophysical Research Letters

Supporting Information for

Impact of spreading rate and age-offset on oceanic transform fault morphology

Yu Ren[1], Jacob Geersen[2], and Ingo Grevemeyer[1]

[1] GEOMAR Helmholtz Centre for Ocean Research Kiel, Wischhofstr. 1-3, 24148 Kiel, Germany

[2] Institute of Geosciences, University of Kiel, Otto-Hahn-Platz1, 24118 Kiel, Germany

Corresponding author: Yu Ren (yren@geomar.de)

Contents of this file

Additional Supporting Information (Files uploaded separately)

Text S1. Comparison with recent statistics on transform morphology

After the discovery of OTFs in the mid-1960s (Wilson, 1965), it has been recognized that OTFs show a vast variability in their morphology, which is partly related to advances in the quality and quantity of seafloor mapping. Previous statistical investigations of transform morphology usually focused on the length (Sandwell, 1986; Luo et al., 2021), width (Searle, 1986; Dauteuil et al., 2002; Mishra & Gordon, 2016; Luo et al., 2021), and depth (Luo et al., 2021; Grevemeyer et al., 2021) of OTFs. However, it should be noted that most previous approaches to systematically quantify transform morphology suffer from the incompleteness of shipborne bathymetric datasets putting limitations to (A) the number of analyzed cases, (B) the exact shape of the structural elements, and (C) the quantification of morphological variations within one transform system including the robust assignment of uncertainties (e.g. standard deviation).

For example, the most recent and up-to-date analysis of transform morphology conducted by Luo et al. (2021), is based on the SRTM15+ grid (Tozer et al., 2019) which interpolates sparse ship-based bathymetric soundings with bathymetric predictions from gravity models at 15 arc-seconds spatial resolution. As a consequence, the width of 44 OTFs (all with a relatively simple morphology) was extracted exclusively for the mid-point of the transform valley, ignoring any along-transform variation. Furthermore, the depth of some OTFs was derived from predicted bathymetry (e.g., Charlie Gibbs, Doldrums, Jan Mayen, Marie Celeste, etc.) by averaging depth values along a profile, which cannot resolve short-wavelength depth variation within the transform. Another recent study, which was based exclusively on shipborne data (Grevemeyer et al., 2021), indicated that transform depth correlates with spreading rate and age-offset, but the number of investigated cases (41) was smaller compared to this study (94).

In Figure S5 we systematically compared our results to the above-mentioned statistical datasets on transform morphology from Mishra & Gordon (2016), Luo et al. (2021), and Grevemeyer et al. (2021). The misfit between the different datasets is significant with respect to the width (Figures S5c-d). The width estimates from Luo et al. (2021) are much larger, resulting from the fact that they included the walls of the transform valley, which are generally not considered when investigating the transform deformation zones (e.g., Searle, 1986; Mishra & Gordon, 2016; Grevemeyer et al., 2021). Furthermore, their single width estimates, which were exclusively done for the central point of the transform valleys, do not account for any along transform changes. However, Mishra & Gordon (2016) derived the width based on a rectangle to approximate the shape of transform deformation zone, producing a dataset that has a similar range but shows larger scatters, when compared to our width estimation. Grevemeyer et al. (2021) fitted relatively simple polygons to the transform valleys, most of which were rectangles. Therefore, our approach of using well-defined polygons to outline the shape of transform valley, from which we extracted the width and depth, as well as their standard deviations, is clearly superior and more advanced than any previous estimation.

With respect to the depth of the floor of the transform valley, our data show clearer trends at larger age-offsets and less scatter compared to Luo et al. (2021) (Figure S5b). While our depth estimates show a similar trend compared to those from Grevemeyer et al. (2021), it has to be noted that their values for the large age-offset Andrew Bain and Romanche transform faults were different (Figure S5b). The latter

results from the incompleteness of coverage of shipborne bathymetric data used in their study. For example, the complied bathymetry of Romanche in Grevemeyer et al. (2021) only provided coverage of the east domain, where the transform valley is much deeper. However, our compilation included additional bathymetric data from Ligi et al. (2002) covering the whole transform zone, which resulted in a shallower average depth for the entire transform valley. The same was the case for the Andrew Bain, where Grevemeyer et al. (2021) used a more limited dataset only covering the southern portion of the transform fault.

Therefore, we concluded that our compilation of high-resolution bathymetric data of global OTFs and well-constrained parameterization enables us to present the most complete and advanced dataset on the spreading rate and age-offset dependence of the morphology of OTFs (Table S2; Figure 2).

Text S2. Estimation of the age-offset across OTFs

The lack of high-resolution magnetic data around most OTFs, induces some uncertainties with respect to oceanic crustal ages, that need to be considered when estimating the age offset across a transform fault. Using a global dataset of present-day oceanic crustal ages (e.g. Seton et al., 2020), it is possible to directly derive the age-offset. This method, however, suffers from the above-mentioned incompleteness of magnetic data and may incorporate some gridding artefacts along transform faults and fracture zones (Seton et al., 2020). Alternatively, it is also possible to derive the age offset by dividing the transform length by the half-spreading rate (e.g., Furlong et al., 2001; Luo et al., 2021; Grevemeyer et al., 2021).

To validate and cross-check both methods we first checked the fine-scale quality of the recently published age grid from Seton et al. (2020) for each OTFs. From the investigated 94 OTFs, only 33 show a fine consistency between their geometry and the shapes of the seafloor isochrons. For these 33 cases we extracted the age offset for the two ridge-transform intersections (RTIs) from the Seton et al. (2020) data (Table S1) and compared it to the calculated values from dividing the transform length by the half-spreading rate (Figure S1). The good correlation (Figures S1, S3) between estimated and measured age-offset allows the calculation of age-offset for all OTFs in this study.

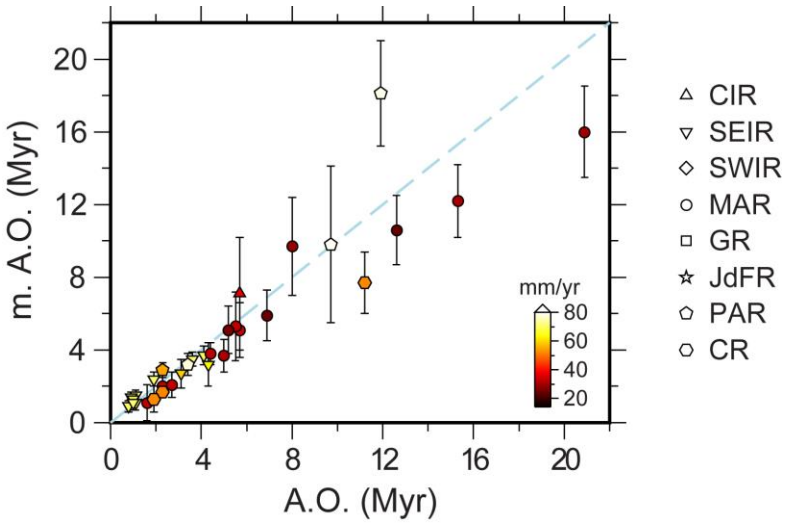

Figure S1. Age-offset from global age model versus calculated age-offset used in the main text. m. A.O., offset in seafloor age across the transform, measured from the global crustal age model (Seton et al., 2020); A.O., offset in seafloor age across the transform, calculated as the transform length divided by half-spreading rate.

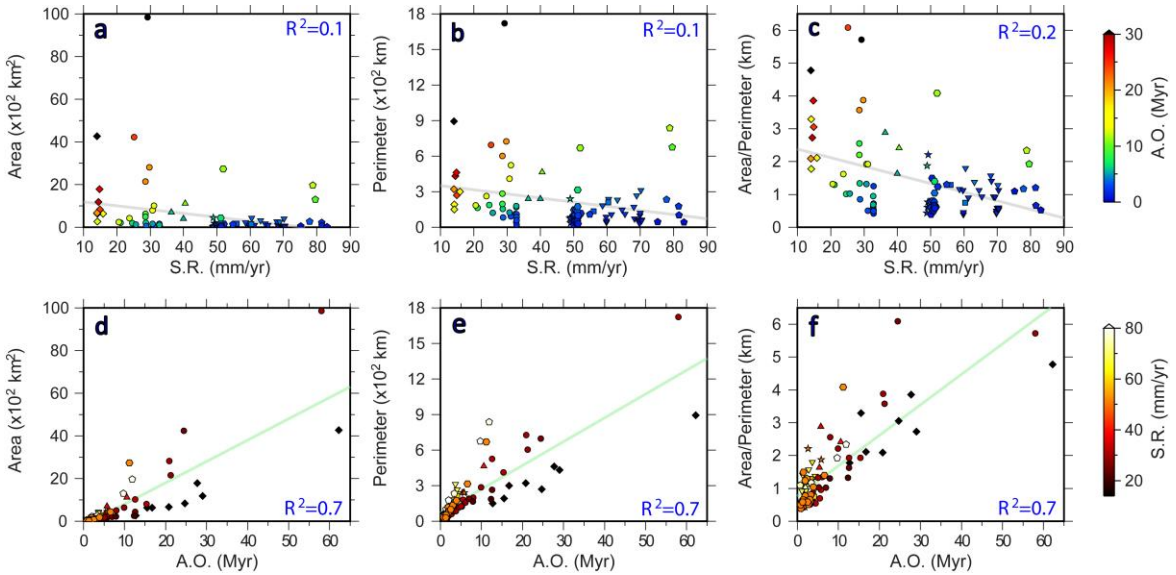

Figure S2. Variations in area, perimeter and area/perimeter ratio of the transform valleys (red polygon in Figure 1b). A.O., age-offset; S.R., spreading rate.

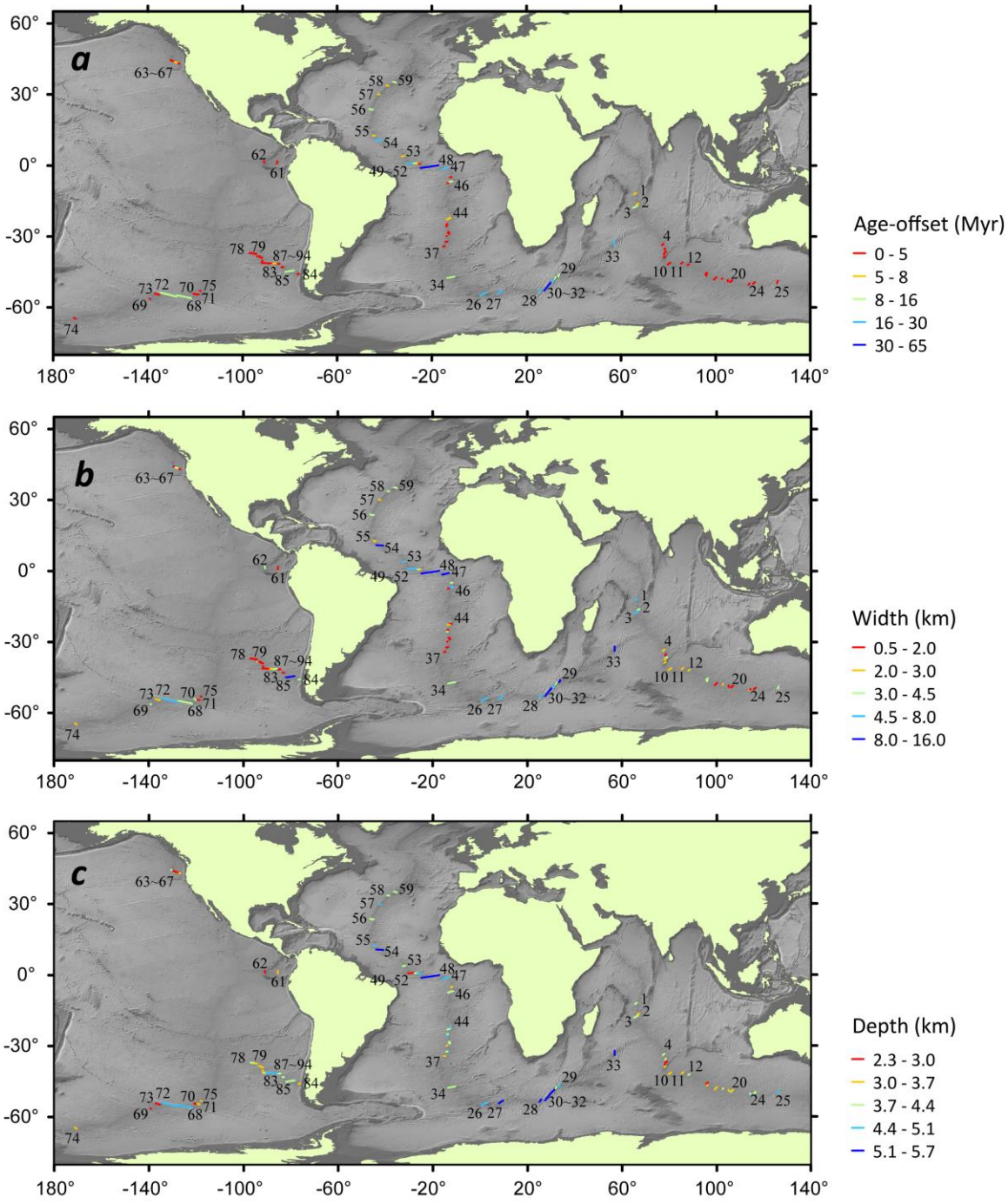

Figure S3. Variation in age-offset, and major morphological parameters (width and depth) of global OTFs. The length of colored lines scales with the length of their corresponding transform faults. Numbering is as in column 1 of Table S2.

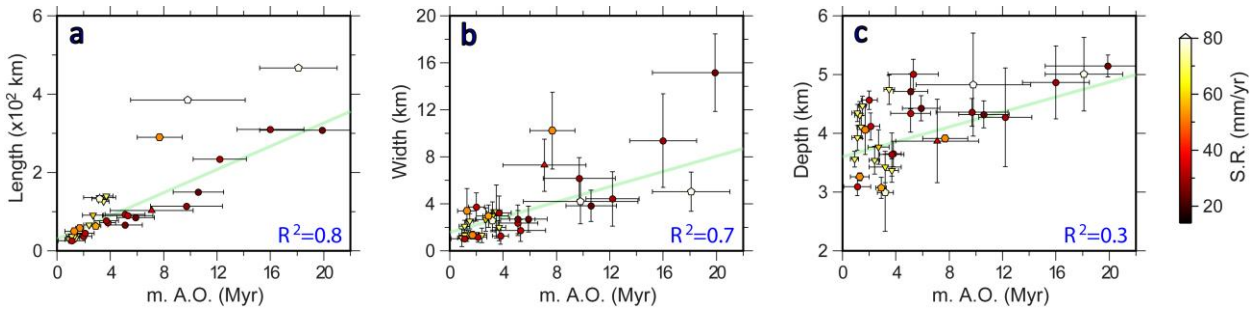

Figure S4. Length, width, and depth of OTFs versus age-offset measured from the global crustal age model (Seton et al., 2020). Only 33 OTFs were shown in the plots due to the quality of global age grids. m. A.O., age-offset measured from global crustal age model.

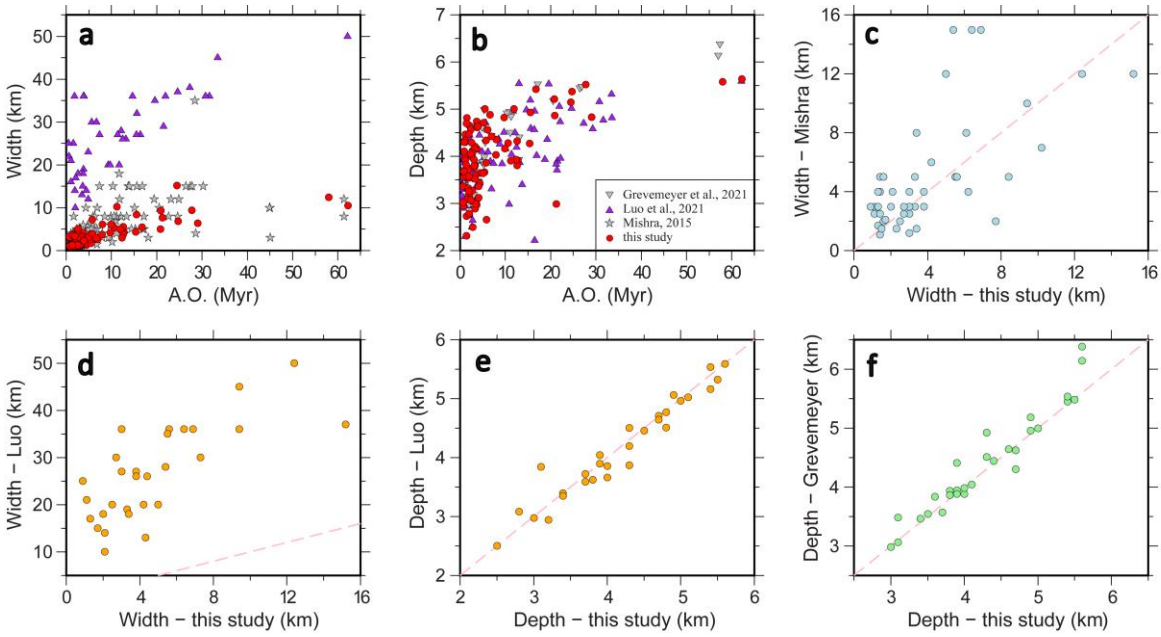

Figure S5. Cross plots of the recent statistical studies (Mishra & Gordon, 2016; Luo et al., 2021; Grevemeyer et al., 2021) and our datasets on the width and depth of OTFs. Dashed pink lines show one-to-one relationship between different datasets.

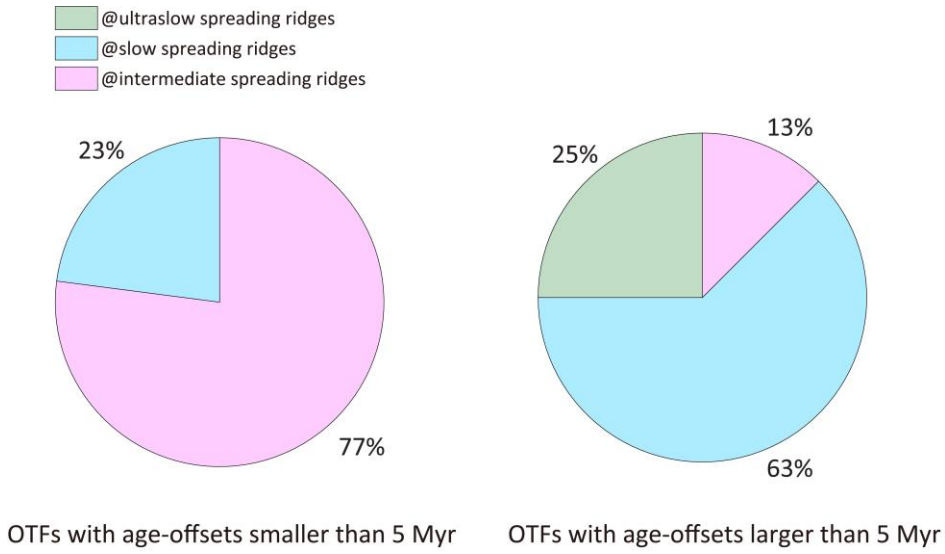

Figure S6. Percentage of different spreading rates for small and large age-offset OTFs, respectively.

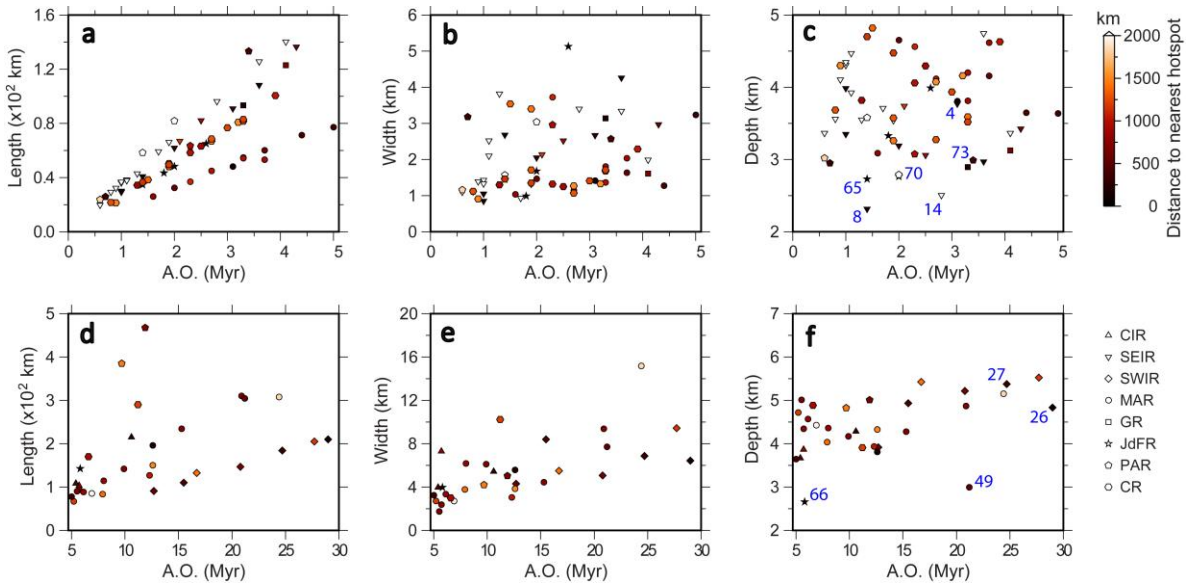

Figure S7. Variations in morphological parameters of OTFs with respect to the effect from nearby hotspot. Hotspot locations were compiled in Table S6. 4, Ter Tholen; 8, Boomerang; 14, SEIR 96E W; 26, Bouvet; 27, Shaka; 49, St Paul A; 65, Blanco C; 66, Blanco D; 70, Raitt W; 73, Hollister.

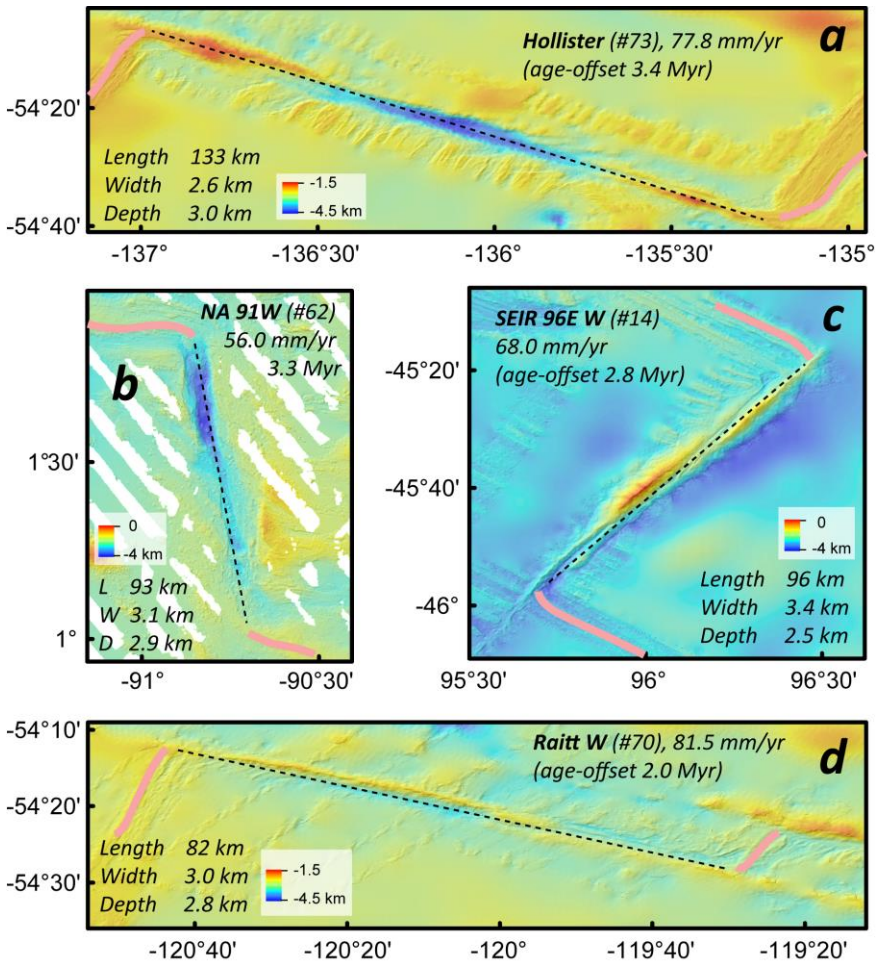

Figure S8. Bathymetric maps of **a,** Hollister (#73), **b,** NA 91W (#62), **c,** SEIR 96E W (#14) and **d,** Raitt W transforms (#70). Locations of the OTFs can be traced in Figure 1a, according to their numbering. Pink thick lines indicate mid-ocean ridges segmented by transform faults. Black dashed lines show the long axis of the OTFs.

OTFs	AO A[a] (Myr)	Unc. A[b] (Myr)	AO B[c] (Myr)	Unc. B[d] (Myr)	Avg. AO[e] (Myr)	Avg. unc.[f] (Myr)
CIR 12S	6.03	2.39	8.07	3.72	7.05	3.06
Ter Tholen	2.87	0.52	2.56	1.02	2.72	0.77
Vlamingh	2.86	1.48	3.51	0.88	3.19	1.18
SEIR 100E	3.83	0.43	3.64	0.48	3.74	0.46
SEIR 103E	1.08	0.34	1.06	0.35	1.07	0.35
SEIR 105E W	0.83	0.33	0.86	0.31	0.85	0.32
SEIR 106E E	1.71	0.38	3.11	0.38	2.41	0.38
Zeehaen W	2.08	0.31	0.82	0.32	1.45	0.32
Zeehaen E	1.67	0.32	1.09	0.36	1.38	0.34
Heemskerck W	1.58	0.34	0.98	0.36	1.28	0.35
Heemskerck E	1.03	0.36	1.16	0.36	1.10	0.36
Euroka	3.34	0.36	3.72	0.41	3.53	0.39
Falkland	11.45	1.05	12.92	2.88	12.19	1.97
MAR 34S	4.77	0.41	2.76	0.77	3.77	0.59
MAR 2945S	1.20	1.15	1.06	0.86	1.13	1.01
MAR 2550S	1.64	0.61	2.34	0.51	1.99	0.56
MAR 25S	2.14	0.56	2.08	0.74	2.11	0.65
MAR 22S W	5.08	2.54	5.18	0.44	5.13	1.49
MAR 22S E	4.88	1.32	5.72	2.42	5.30	1.87
Chain	17.81	2.02	14.11	3.05	15.96	2.54
Strakhow	11.94	3.84	7.36	1.45	9.65	2.65
Vema	19.37	6.52	20.44	2.91	19.91	4.72
Marathon	5.63	1.35	6.09	1.51	5.86	1.43
Kane	9.51	2.34	11.77	1.46	10.64	1.90
Atlantis	5.38	1.06	4.78	1.46	5.08	1.26
MAR5S	3.75	0.96	3.67	0.84	3.71	0.90
Heezen	13.15	5.63	6.53	2.89	9.84	4.26
Tharp	15.43	0.93	20.83	4.88	18.13	2.91
Hollister	3.17	0.91	3.20	0.3	3.19	0.61
Pitman	2.89	0.46	2.91	0.28	2.90	0.37
Chiloe	1.67	0.31	1.62	0.18	1.65	0.25
Darwin	1.52	0.86	1.13	0.53	1.33	0.70
Guafo	7.43	2.09	8.00	1.25	7.72	1.67

Table S1. Age-offset across OTFs from global age model (Seton et al., 2020).

[a] Age-offset measured at one RTI

[b] Uncertainty of the age-offset in [a]

[c] Age-offset measured at the other RTI

[d] Uncertainty of the age-offset in [b]

[e] Mean value of age-offsets estimated at the two RTIs

[f] Averaged uncertainty for the age-offset

Table S2. Morphological characteristics of global oceanic transform faults (details in the extended excel spreadsheet).

Type	Spreading Rate (mm/yr)	Age-offset (Myr)	Length (km)	Width (km)	Depth (km)
Ultraslow	14.6	26.2	189.7	7.1	5.1
Slow	39.1	6.7	117.4	4.1	3.8
Intermediate	63.0	3.2	100.7	2.4	3.5

Table S3. Averaged morphological parameters of the 94 transform faults from ultraslow- to intermediate-spreading ridges.

Correlations	R^2	Adjusted R^2	RMSE	SSE
L vs. SR	0.05	0.04	114.89	1.21e+06
W vs. SR	0.25	0.24	3.37	1.05e+03
D vs. SR	0.22	0.21	0.40	14.61
L vs. AO	0.69	0.69	65.74	3.98e+05
W vs. AO	0.58	0.58	2.52	584.78
D vs. AO	0.39	0.38	0.35	11.46
L vs. AO (> 5 Myr)	0.54	0.53	108.73	3.55e+05
W vs. AO (> 5 Myr)*	0.69	0.68	2.30	143.34
D vs. AO (> 5 Myr)*	0.49	0.47	0.28	2.24

*OTFs that have undergone obvious secondary processes with numbering (Table S4) were excluded in the calculation, as mentioned in Figures 2k-l.

Table S4. The summary statistics of weighted linear fits in Figure 2. L, length; W, width; D, depth; SR, spreading rate; AO, age-offset; R^2, coefficient of determination; Adjusted R^2, adjusted coefficient of determination; RMSE, root mean squared error; SSE, sum of squares due to error.

OTFs	AO (Myr)	Width (km)	Depth (km)	Tectonic features
CIR 12S (#1)	7.1	7.284	3.870	Nearby Rodriguez hotspot (triple junction)
St Paul A (#49)	17.7	7.709	2.990	Nearby Fernando hotspot; PMC (Maia et al., 2016)
Vema (#54)	19.0	15.174	5.147	Transtension caused by PMC (Bonatti et al., 2005)
Blanco D (#66)	5.8	3.981	2.658	Nearby P. Jackson hotspot; PMC (Wilson, 1993)
Guafo (#85)	7.5	10.224	3.912	Transtension possibly from PMC (Tebbens et al., 1997)

Table S5. Parameters and secondary processes of the obvious outliers in Figures 2h-i. PMC, plate-motion change.

Hotspot	Lon. (º)	Lat. (º)	Hotspot	Lon. (º)	Lat. (º)	Hotspot	Lon. (º)	Lat. (º)
Afar	39.5	7.0	E. Australia	146.0	-40.8	Marqueses	-139.0	-10.5
Aitutaki	-159.8	-18.9	Eifel	6.7	50.2	Martin	-28.8	-20.5
Amsterdam	77.0	-37.0	Erebus	167.2	-77.5	Massif Central	2.7	45.1
Anyuy	166.0	67.0	Etna	15.0	37.8	Meteor	1.0	-51.4
Arago	-150.7	-23.4	Fernando	-32.4	-3.8	Mt. Rungwe	33.9	-8.3
Arnold	-25.0	-18.0	Foundation	-111.1	-37.7	New England	28.0	-32.0
Ascension	-14.3	-7.9	Galapagos	-91.6	-0.4	North Austral	-143.3	-25.6
Azores	-26.0	37.9	Gough	-10.0	-40.3	Ob-Lena	40.0	-52.2
Baikal	101.0	51.0	Great Meteor	28.0	30.0	Peter I	-90.6	-68.8
Baja	-114.5	27.7	Guyana	-61.0	5.0	Pitcairn	-129.3	-25.4
Balleny	164.8	-67.6	Hainan	110.0	20.0	P. Jackson	-127.7	42.5
Bermuda	-64.3	32.6	Hawaii	-155.2	19.0	Rarotonga	-159.0	-21.5
Bouvet	3.4	-54.4	Heard	73.5	-53.1	Raton	-104.1	36.8
Bowie	-134.8	53.0	Hoggar	5.6	23.3	Reunion	55.7	-21.2
Cameroon	5.1	-2.0	Hollister	-219.0	-54.0	Rodriguez	63.5	-19.6
Canary	-18.0	28.2	Iceland	-17.3	64.4	Sala Gomez	-109.0	-27.0
Cape Verde	-24.0	16.0	Jan Mayen	-8.2	71.1	Samoa	-169.1	-14.5
Caroline	164.4	4.8	Jebel Marra	24.2	13.0	San Felix	-80.1	-26.4
Christmas	80.0	-35.0	Juan de Fuca	231.0	45.0	Scott	-178.8	-68.8
Circe	-9.0	-8.0	J. Fernandez	-81.8	-33.9	Shimada	-117.5	16.9
Cobb	-130.1	46.0	Karisimbi	29.4	-15	Shona	6.0	-52.0
Cocos	94.5	-17.0	Kerguelen	69.0	-49.6	Socorro	-111.0	18.7
Comores	43.3	-11.5	Kilimanjiro	37.5	-3.0	St. Helena	-9.5	-16.5
Corner	-51.5	36.5	Lord Howe	159.8	-34.7	Tahiti/Society	-148.4	-18.2
Crough	-114.6	-26.9	Louisville	-140.6	-53.6	Tasmanid	155.5	-40.4
Crozet	50.2	-46.1	Macdonald	-140.3	-29.0	Tibesti	17.5	20.8
Darfur	24.0	13.0	Madeira	-17.3	32.6	Tristan	-12.3	-37.2
Discovery	-2.7	-43.0	Maria	-154.0	-22.2	Vema	6.3	-32.1
East Africa	34.0	6.0	Marion	37.6	-46.9	Yellowstone	-110.4	44.5
Easter	-106.5	-26.4	M.-Gilbert	-153.5	-21.0			

Table S6. Location of the hotspots used in this paper (modified from the "Compleate Hot Spot Table" via http://www.mantleplumes.org/CompleateHotspotTable.xls, and Morgan & Morgan, 2007).